ARL-TR-9092 ● Oct 2020

DEVCOM ARMY RESEARCH LABORATORY

MidIR and LWIR Thermal Polarimetric Imaging Comparison using Receiver Operating Characteristic (ROC) Curve Analysis

by Kristan P Gurton and Richard Edmondson

NOTICES

Disclaimers

The findings in this report are not to be construed as an official Department of the Army position unless so designated by other authorized documents.

Citation of manufacturer's or trade names does not constitute an official endorsement or approval of the use thereof.

Destroy this report when it is no longer needed. Do not return it to the originator.

ARL-TR-9092 ● OCT 2020

MidIR and LWIR Thermal Polarimetric Imaging Comparison using Receiver Operating Characteristic (ROC) Curve Analysis

Kristan P Gurton
Computational and Information Sciences Directorate, CCDC Army Research Laboratory

Richard Edmondson
Polaris Sensor Technology

REPORT DOCUMENTATION PAGE

Form Approved
OMB No. 0704-0188

1. REPORT DATE *(DD-MM-YYYY)*	2. REPORT TYPE	3. DATES COVERED (From - To)
October 2020	Technical Report	19 January–14 September 2020

4. TITLE AND SUBTITLE
MidIR and LWIR Thermal Polarimetric Imaging Comparison using Receiver Operating Characteristic (ROC) Curve Analysis

5a. CONTRACT NUMBER

5b. GRANT NUMBER

5c. PROGRAM ELEMENT NUMBER

6. AUTHOR(S)
Kristan P Gurton and Richard Edmondson

5d. PROJECT NUMBER

5e. TASK NUMBER

5f. WORK UNIT NUMBER

7. PERFORMING ORGANIZATION NAME(S) AND ADDRESS(ES)
CCDC Army Research Laboratory
ATTN: FCDD-RLC-ES
Adelphi, MD 20783-1138

8. PERFORMING ORGANIZATION REPORT NUMBER
ARL-TR-9092

9. SPONSORING/MONITORING AGENCY NAME(S) AND ADDRESS(ES)

10. SPONSOR/MONITOR'S ACRONYM(S)

11. SPONSOR/MONITOR'S REPORT NUMBER(S)

12. DISTRIBUTION/AVAILABILITY STATEMENT
Approved for public release; distribution is unlimited.

13. SUPPLEMENTARY NOTES

14. ABSTRACT
We report results from a field-test study to assess target detection capabilities for both mid-IR (MidIR) and long-wave IR (LWIR) polarimetric camera systems that was held during the week of January 19–23, 2020, at Fort Hunter Liggett, California. In particular, we analyze detection ability for a stationary target, over a prolonged period, in which receiver operating characteristic (ROC) curve analysis was applied to the resultant thermal and polarimetric imagery recorded by both sensors. Imagery considered includes conventional MidIR and LWIR thermal radiance, S0 images, as well as Stokes imagery (i.e., S1, S2), and degree-of-linear polarization (DoLP) for both wavebands. Both polarimetric imaging systems used Stirling cooled focal-plane arrays that were based on mercury cadmium telluride or indium antimonide substrates, with pixel densities of 640×480 and 1280×1024 for the LWIR and MidIR sensors, respectively. ROC curve analysis showed improved target detection for DoLP images for both wavebands when compared to conventional thermal imagery, S0 (W/(sr*m^2)).

15. SUBJECT TERMS
polarimetric, thermal imaging, target detection, polarimetry, mid-IR, MidIR, long-wave IR, LWIR

16. SECURITY CLASSIFICATION OF:			17. LIMITATION OF ABSTRACT	18. NUMBER OF PAGES	19a. NAME OF RESPONSIBLE PERSON
a. REPORT	b. ABSTRACT	c. THIS PAGE			Kristan P Gurton
Unclassified	Unclassified	Unclassified	UU	29	19b. TELEPHONE NUMBER (Include area code) (301) 394-2093

Contents

List of Figures iv

List of Tables v

1. Introduction 1

2. MidIR and LWIR Polarimetric Sensors 2

3. Polarimetric Methodology 5

4. ROC Curve Analysis 7

5. Field Test 9

6. ROC Curve Results 9

7. Results and Conclusion 15

8. References 19

List of Symbols, Abbreviations, and Acronyms 21

Distribution List 22

List of Figures

Fig. 1 LWIR thermal (left) and polarimetric DoLP (right) image comparison of Soldiers recorded at Ft Hunter Liggett 2

Fig. 2 LWIR thermal (left) and polarimetric DoLP (right) image comparison of a Russian 1970s vintage T-72 tank..... 2

Fig. 3 LWIR MCT polarimetric camera system based on the SAR design 3

Fig. 4 Cross section of the MidIR polarimeter with the a) long-range objective mounted and b) 25-mm objective mounted..... 4

Fig. 5 Typical scene considerd for ROC curve analysis (left). In this LWIR scene, a T-72 tank is centrally located in the foreground and serves as the target of interest. The image on the right is a magnified portion in which an ROI is defined and used in the ROC analysis. 8

Fig. 6 a) A simple image histogram where the target and background regions are clearly defined and b) the corresponding ROC curve, where the area under the curve is related to the probability to detect a target within the image scene..... 8

Fig. 7 Image of the test site for January 23, 2020, recorded at 17:50 showing overcast conditions that steadily thickened as cloud formations grew throughout the test period 9

Fig. 8 ROC curve (left) and corresponding LWIR S0 image recorded at 17:50 10

Fig. 9 ROC curve (left) and corresponding LWIR S0 image recorded at 20:48 10

Fig. 10 ROC curve (left) and corresponding LWIR S1 image recorded at 17:50 11

Fig. 11 ROC curve (left) and corresponding LWIR S1 image recorded at 20:48 11

Fig. 12 ROC curve (left) and corresponding LWIR S2 image recorded at 17:50 11

Fig. 13 ROC curve (left) and corresponding LWIR S2 image recorded at 20:48 11

Fig. 14 ROC curve (left) and corresponding LWIR DoLP image recorded at 17:50 12

Fig. 15 ROC curve (left) and corresponding LWIR DoLP image recorded at 20:48 12

Fig. 16 ROC curve (left) and corresponding MidIR S0 image recorded at 18:30 12

Fig. 17 ROC curve (left) and corresponding MidIR S0 image recorded at 20:48 13

Fig. 18. ROC curve (left) and corresponding MidIR S1 image recorded at 18:30 13
Fig. 19 ROC curve (left) and corresponding MidIR S1 image recorded at 20:48 13
Fig. 20 ROC curve (left) and corresponding MidIR S2 image recorded at 18:30 14
Fig. 21 ROC curve (left) and corresponding MidIR S2 image recorded at 20:48 14
Fig. 22 ROC curve (left) and corresponding MidIR DoLP image recorded at 18:30 14
Fig. 23 ROC curve (left) and corresponding MidIR DoLP image recorded at 20:48 15
Fig. 24 DoLP as a function of time for both MidIR and LWIR wavebands and corresponding trend lines (dashed curve) 17
Fig. 25 Measured LWIR background and target radiance values (W/sr*m^2) as a function of time recorded during January 23, 2020 18
Fig. 26 Measured MidIR background and target radiance values (W/sr*m^2) as a function of time recorded during January 23, 2020 18

List of Tables

Table 1 Key parameters for the LWIR SAR polarimetric camera system..... 3
Table 2 Key parameters for the MidIR DoA-SAR hybrid polarimetric sensor . 5
Table 3 Results of ROC curve analysis for early evening and late evening, for all radiance and polarimetric imagery shown in Figs. 8–23 15

1. Introduction

Polarimetric imaging is the generation of a 2-D image (or video) whose pixel value is directly related to the *polarization state* of the image-forming light. This novel imaging methodology has been explored to varying degrees in the past where the primary mode of operation was limited to the visible or near-IR (NIR) regions of the spectrum.[1–4] However, there has been recent development within the DOD and private sector research communities in which a series of "research-grade" long-wave IR (LWIR) and mid-IR (MidIR) polarimetric imaging sensor systems have been developed.[5–8]

Polarimetric sensors that operate in the thermal IR are designed to exploit the phenomenon that "manmade" objects emit thermal radiation that tends to have a preferential polarization state (usually linear), while naturally occurring "background" materials (e.g., vegetation, grass, trees, and so on) tend to show little or no preferential polarization. As a result, a thermal polarimetric image can significantly enhance the ability to detect certain targets by increasing the contrast between manmade objects and their respective background, while simultaneously suppressing non-polarized clutter. Example applications for using polarimetric imaging in thermal IR include detection of disturbed earth and/or altered road surfaces, enhanced targeting and tracking of manmade vehicles and personnel, the identification/suppression of military decoys, and the improved remote detection of hidden or camouflaged objects.[9–12]

Because a thermal polarimetric image contains both conventional thermal and polarization information, when augmented, the resultant scene tends to display much more fine detail when compared to conventional thermal only. Examples of this improved information content can be seen in Figs. 1 and 2. Each image pair shown in Figs. 1 and 2 displays a conventional LWIR thermal picture (left) and the resultant polarimetric degree-of-linear polarization (DoLP) image (right). As one can see, much of the fine detail in the thermal image (left) appears washed out and not resolved, while the polarimetric product DoLP image (right) displays more spatial detail and resolution.

Fig. 1 LWIR thermal (left) and polarimetric DoLP (right) image comparison of Soldiers recorded at Ft Hunter Liggett

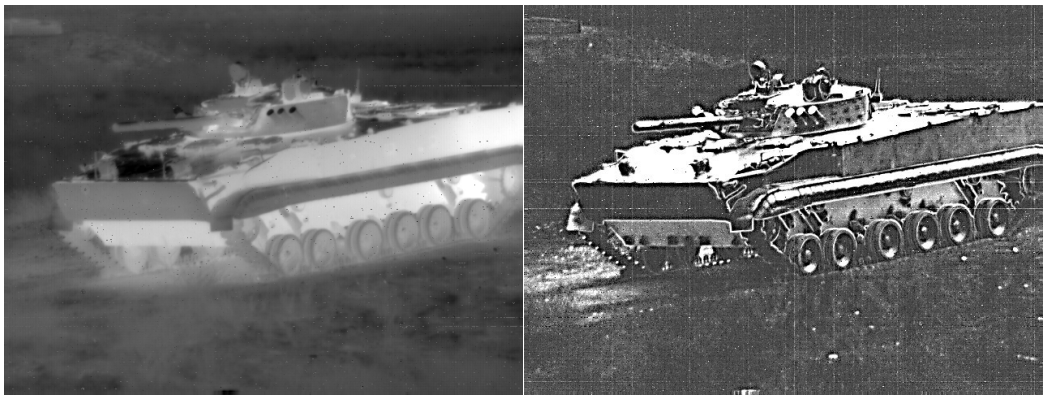

Fig. 2 LWIR thermal (left) and polarimetric DoLP (right) image comparison of a Russian 1970s vintage T-72 tank

2. MidIR and LWIR Polarimetric Sensors

For this test, we considered two polarimetric sensors, each functioning in a different waveband region of the IR spectrum: a MidIR (3.7–4.9 μm) and a LWIR (7.5–11.1 μm) camera system. The LWIR system utilized Stirling cooled, mercury cadmium telluride (MCT) focal-plane arrays (FPAs), with pixel densities of 640 × 480, while the MidIR platform uses "two" indium antimonide (InSb) FPAs, each with pixel densities of 1280 × 1024; however, each polarimetric camera used a different optical configuration to accomplish the necessary polarimetric filtering.

Both systems were acquired from Polaris Sensor Technologies Inc. (Huntsville, Alabama), in which the LWIR polarimetric camera was based on a spinning-achromatic-retarder (SAR) design, while the MidIR platform used a two-camera, division-of-amplitude (DoA), SAR hybrid optical design.[13–15]

The LWIR SAR polarimetric camera shown in Fig. 3 uses a rapidly spinning achromatic phase-retarder that is mounted in series with a linear polarizer. A

"sequence" of images are recorded at a 120-Hz frame rate, where each image represents a particular polarization state. A Fourier modulation technique is applied to the pixel readout in which a Fourier series expansion is calculated for each channel. Finally, the expansion is inverted to yield the Stokes image parameters in terms of Fourier coefficients, which are used to generate the desired Stokes image. This LWIR polarimetric system was equipped with a dual-focus objective, with a 45- and 145-mm optic, resulting in a field of view (FOV) of 10.6° × 7.9° and 3.3° × 2.5°, respectively. Additional key parameters are listed in the Table 1.

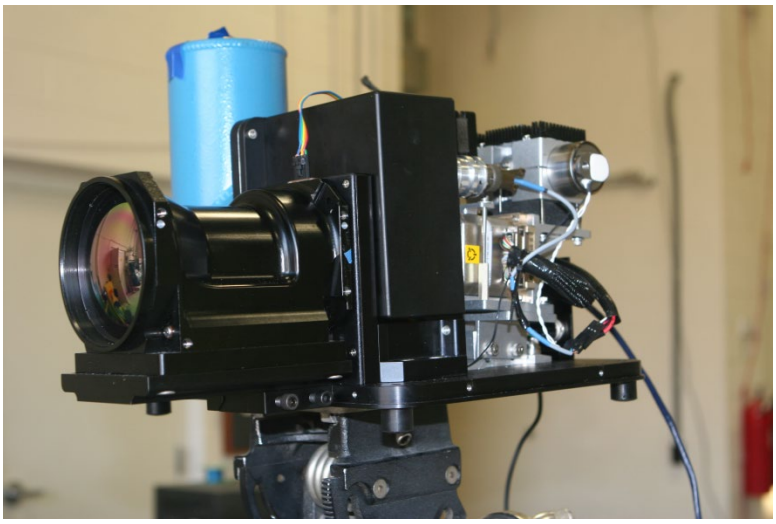

Fig. 3 LWIR MCT polarimetric camera system based on the SAR design

Table 1 Key parameters for the LWIR SAR polarimetric camera system

Parameter	Specification
Format	640 × 480
Waveband	7.5–11.1 μm
Pixel size	15-μm square
NEΔT	25 mK at f/2
NEΔDoLP	0.1%
Frame rate	120 Hz
Dynamic range	14 bit
Narrow FOV	3.3° × 2.5°
Wide FOV	10.6° × 7.9°
Pixel size	15 × 15 μm
IFOV at 1 km	(narrow FOV) 4 inches, (wide FOV) 12 inches

Note: IFOV = instantaneous FOV.

The polarimetric filtering architecture used for the MidIR sensor is a DoA SAR hybrid system that captures two orthogonal states by splitting the scene using a polarimetric beam-splitting cube. Each state is then projected to one of the two InSb FPAs. The image-forming radiance enters the system and passes through a half-

wave achromatic retarder. The vertically polarized radiance emerging from the half-wave retarder is transmitted through the polarizing beam-splitter cube, and the horizontally polarized light is reflected off the hypotenuse face of the polarizing beam-splitter cube.

When the system is operated, the half-wave retarder is rotated continuously. During the integration time, the retarder sweeps through a finite range of angles depending on the integration time and frame rate. For example, if a 4-ms integration time is chosen with a 60-Hz frame rate, then the retarder sweeps through an angle of ($4x10{-}3 \times 60 \times 22.5° = 5.40$). The intensity modulation caused by the rotation of the half-wave retarder is reduced by a small amount of 0.8%. For most operations, the integration time will be around 7 ms. Thus, the polarization contrast is not impacted by the continuous rotation of the retarder. The system is provided with objectives, one long range of 600 mm and one short range of 25 mm, which are quickly interchangeable. Pictures of the MidIR DoA SAR hybrid system with the 600- and 25-mm objectives mounted are shown in Fig. 4a and b, while key parameters for the MidIR system are listed in Table 2.

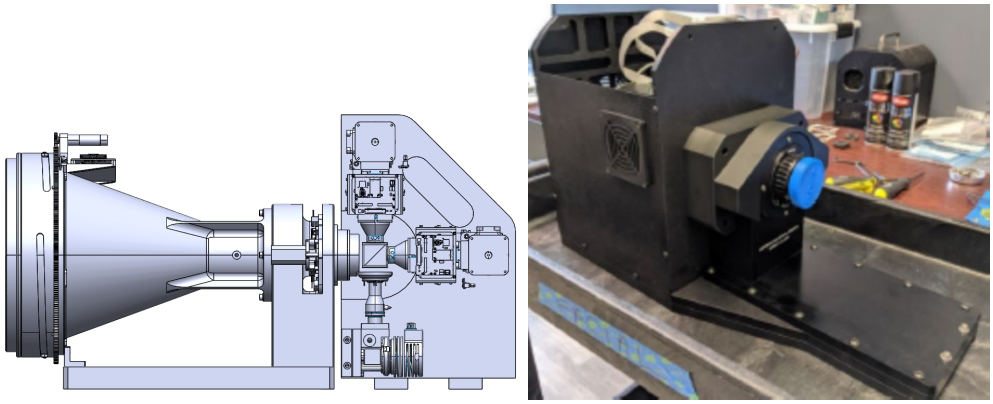

(a) (b)

Fig. 4 Cross section of the MidIR polarimeter with the a) long-range objective mounted and b) 25-mm objective mounted

Table 2 Key parameters for the MidIR DoA-SAR hybrid polarimetric sensor

Parameter	Value
Detector	InSb 2-D array
Waveband	3.7–4.8 µm
Resolution (H x V)	1280 × 1024 pixels
Pixel pitch	10 µm
EFL	600 mm, 25 mm
F/#	3
Horizontal FOV	1.22° (600 mm), 28.72° (25 mm)
IFOV	16.8 µRad (600 mm), 396.6 µRad (25 mm)
Frame rate	50 Hz
Focus	Motorized (600 mm), Manual (25 mm)
Bit depth	13 bit
NEDT	28 mK
NEDoLP	0.14%
Size (L × W × H)	25.5 × 10 × 13.5 inches (600 mm), 22.8 × 10 × 13.5 inches (25 mm)
Weight	60 lb (600 mm), 45 lb (25 mm)
Input power supply	24 VDC at 10 A
Data interface	USB 3.0

Note: NEDT = noise equivalent differential temperature,
NEDoLP = noise equivalent DoLP.

3. Polarimetric Methodology

For polarimetric applications, it is common practice to use a Stokes parameter approach to describe the polarization state of the image-forming radiation that results from either emission or reflection.[16] We apply the Stokes parameter methodology to our imaging application, where we define the Stokes parameters images S1, S2, and S0 by Eqs 1–3:

$$S1 = I(0) - I(90) \quad (w/sr\text{-}m^2), \tag{1}$$

$$S2 = I(+45) - I(-45) \quad (w/sr\text{-}m^2), \tag{2}$$

$$S0 = \text{total calibrated radiance image} \quad (w/sr\text{-}m^2), \tag{3}$$

and the DoLP as

$$\text{DoLP} = \frac{\sqrt{S1^2 + S2^2}}{S0}, \tag{4}$$

where I(0), I(90), I(+45), and I(–45) represent 2-D LWIR images produced with polarimetrically filtered radiance that is polarized (relative to the vertical plane) at 0°, 90°, +45°, or –45°, respectively. As one can see from Eqs. 1–3, the S1 image represents a measure of the vertical state as compared to the horizontal state, the S2 image represents a measure of the difference between the two ±45° diagonal states, and the combined radiance image, S0, is taken to be equivalent to the conventional LWIR thermal image. Finally, it is common practice to normalize S1 and S2 with respect to S0 in order to generate a unitless fraction—S1(%)=100 × (S1/S0) and S2(%)=100 × (S2/S0)—and this is the convention we use throughout this report.

Because we are comparing detection responses between two different waveband regions (MidIR versus LWIR), it is informative to understand polarization states due to either *reflection* or *emission* combined and yield the *net* polarimetric response of the sensor.

Generally, induced polarization, either by reflection of ambient radiation off the target or thermal-induced emission from the target, arises from the fact that both parameters are directionally dependent quantities: $\rho(\lambda,\theta,\phi)$ and $\varepsilon(\lambda,T,\theta,\phi)$, where ρ and ε are the directional reflection and emission coefficients, respectively. As a result, the values of these quantities change depending on how they are viewed relative to angles θ and ϕ, which are directions defined relative to a surface normal, $\hat{n}$. Taking these formulations into account, one can rewrite each quantity in terms of a superposition of orthogonal components, as shown in Eqs. 5 and 6:

$$\rho(\lambda,\theta,\phi) = \frac{\rho_{\perp}(\lambda,\theta)+\rho_{\parallel}(\lambda,\theta)}{2} \qquad \text{Total reflectivity} \qquad (5)$$

$$\varepsilon(\lambda,T,\theta,\phi) = \frac{\varepsilon_{\perp}(\lambda,T,\theta)+\varepsilon_{\parallel}(\lambda,T,\theta)}{2} \qquad \text{Total emissivity} \qquad (6)$$

As a result, the DoLP due to reflection, $DOLP_{\rho}$, and emission, $DOLP_{\varepsilon}$, can be expressed as in Eqs. 7 and 8:

$$DOLP_{\rho} = \frac{(\rho_{\perp}(\lambda,\theta)-\rho_{\parallel}(\lambda,\theta)}{(\rho_{\perp}(\lambda,\theta)+\rho_{\parallel}(\lambda,\theta)} \qquad \text{Reflection induced polarization} \qquad (7)$$

$$DOLP_{\varepsilon} = \frac{(\varepsilon_{\perp}(\lambda,\theta)-\varepsilon_{\parallel}(\lambda,\theta)}{(\varepsilon_{\perp}(\lambda,\theta)+\varepsilon_{\parallel}(\lambda,\theta)} \qquad \text{Emission induced polarization} \qquad (8)$$

Although not apparently obvious from Eqs. 7 and 8, the DoLP due to reflection, $DOLP_{\rho}$, is *orthogonal* with respect to the DoLP due to emission, $DOLP_{\varepsilon}$. As a result, when a target exhibits both types of induced polarization states, the *net* total DoLP, $DOLP_{Total}$, recorded by a polarimetric sensor represents a vector superposition of

the two orthogonal states, which serve to oppose (difference) each other, and is represented in Eq. 9:

$$DOLP_{Total} = \left| DOLP_{\rho} - DOLP_{\varepsilon} \right| \qquad \text{“net” polarization state} \quad (9)$$

In practice, one type of induced polarization dominates, resulting in a measureable DoLP signal; however, it is not uncommon to see polarization states “flip”, as evident in the sign of either S1 or S2. For example, consider a warm target heated by clear-sky conditions. In this particular case, we would expect emission-induced polarization to dominate, as the ambient reflected radiance due to the “cold sky” is small compared to the emission of the warm target. Finally, one needs to also consider how ambient atmospheric conditions affect the magnitude of radiant levels for both MidIR and LWIR camera systems. Generally, it is thought the MidIR response is more sensitive to meteorological changes (e.g., cloud cover versus clear sky) compared to the LWIR region, and for common terrestrial ambient temperatures, the received signal is often stronger in LWIR.

4. ROC Curve Analysis

The ROC method was originally developed for radar signal detection analysis, but is now widely applied in many different disciplines.[17–19] ROC curve analysis has been traditionally used to compare target detectability among different images sets recorded or processed by different means. For example, for a particular target, a ROC curve is calculated for each image in a comparison set. To do this, some a priori knowledge is necessary that relates the nature of both the target and its associated background region so that a “truth” image can be generated. This truth image is a defined region of interest (ROI) in which the target in question is outlined (Fig. 5) and the associated background ROI is defined as everything else not located in the ROI of the truth image. Both histograms (plot of pixel values versus number of pixels with each value) for the target and background ROI are measured. Figure 6a represent a simple histogram of the truth image, where the large Gaussian-like curve on the left represents the histogram associated with the background and the vertical line represents an arbitrary “threshold” point.

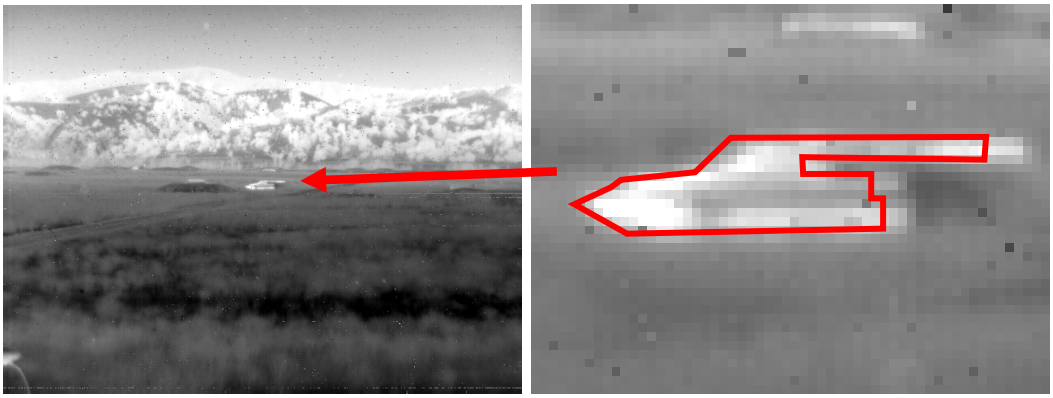

Fig. 5 Typical scene considerd for ROC curve analysis (left). In this LWIR scene, a T-72 tank is centrally located in the foreground and serves as the target of interest. The image on the right is a magnified portion in which an ROI is defined and used in the ROC analysis.

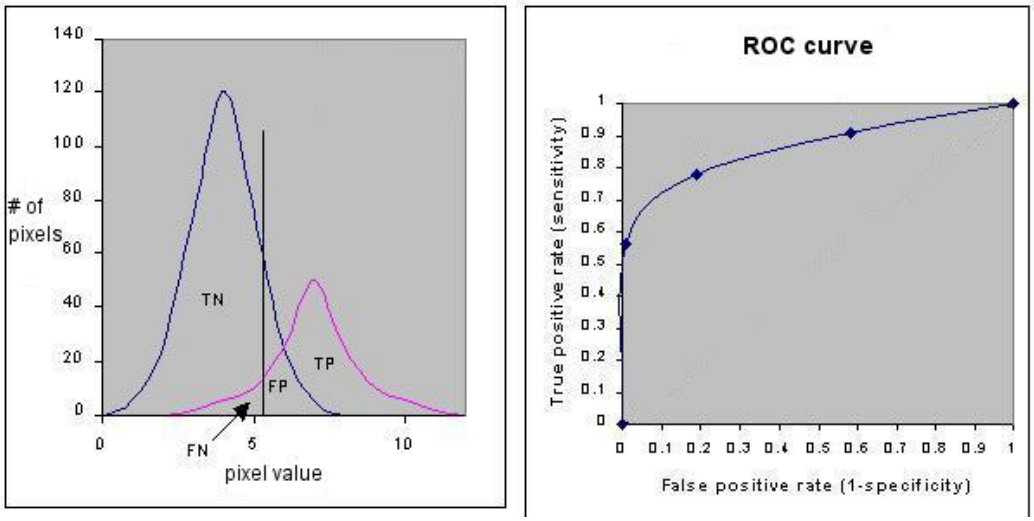

(a) (b)

Fig. 6 a) A simple image histogram where the target and background regions are clearly defined and b) the corresponding ROC curve, where the area under the curve is related to the probability to detect a target within the image scene

A ROC curve is generated by comparing overlapping regions defined as true negative (TN), false positive (FP), and true positive (TP), as the threshold point is swept right to left across the histogram. Figure 6b shows a resultant ROC curve for the histogram(s) shown in Fig. 6a. The area under the ROC curve is defined as the normalized probability of detection for the target set identified in the truth image. An area value of unity represents a 100% probability of detection.

5. Field Test

The field test was conducted during the week of January 19–23, 2020, at Fort Hunter Liggett, California. Atmospheric conditions for most of the test were pleasant yet cool, with temperatures ranging from the low-50s °F in the afternoon, to mid-30s °F in the evening. For our ROC curve analysis, we focused on a 5-h period incorporating the dusk period of January 23, from approximately 17:00 until 21:00. This period was purposely chosen in order to measure system detectability during what is commonly call the "thermal-crossover" period, which occurs typically at the dusk and dawn periods of each day. This cross-over period is considered to be the most challenging period for thermal detection due to the fact the radiant difference between a target and its associated background become similar. During the test period, temperatures started at 49 °F at 17:00 and fell continually to a low of 37 °F by 21:00. During the entire test, we noticed overcast conditions as shown in Fig. 7, which continued to increase with additional cloud formation as the evening went on.

Fig. 7 Image of the test site for January 23, 2020, recorded at 17:50 showing overcast conditions that steadily thickened as cloud formations grew throughout the test period

6. ROC Curve Results

Figures 8–23 show a series of ROC curves for all radiance, S0, and Stokes images, S1 and S2, as well the polarimetric product image DoLP, for the early and late

period of the test day of January 23, 2020. We chose these periods for comparison to highlight the effects of changing temperatures and increasing cloud cover as the test period progressed from approximately 17:50 until 20:48. In addition, the resultant image that was used to calculate the ROC curve is included on the right side of each pair. Included in each ROC curve are the time period of image capture, the particular parameter, and the resultant "area" under the ROC curve, keeping in mind that an area of "1" signifies 100% probability of detection, whereas an area of 0.65 corresponds to a 65% chance of detection. It should be noted due to technical issues with the MidIR system, we were unable to capture complete polarimetric sets of S0, S1, S2, and DoLP until approximately 18:30.

LWIR Results

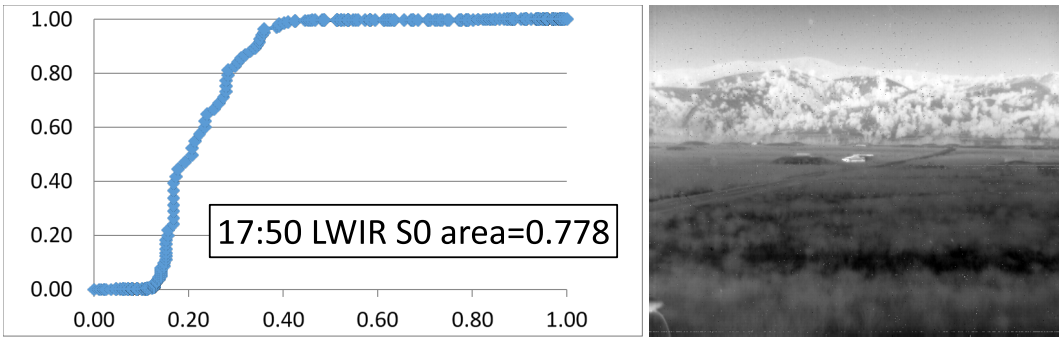

Fig. 8 ROC curve (left) and corresponding LWIR S0 image recorded at 17:50

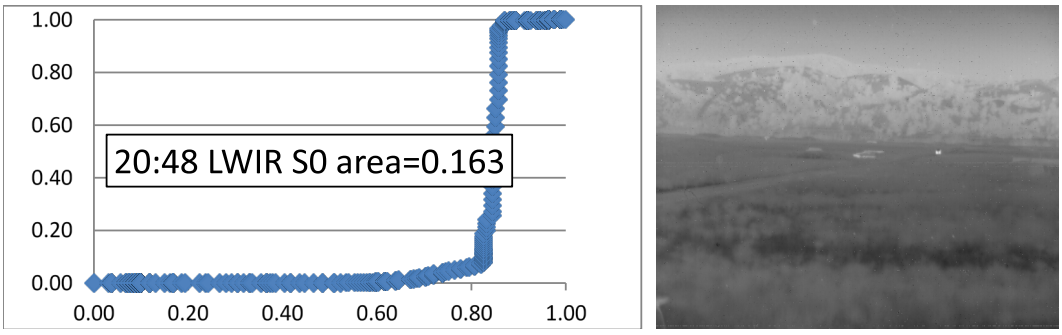

Fig. 9 ROC curve (left) and corresponding LWIR S0 image recorded at 20:48

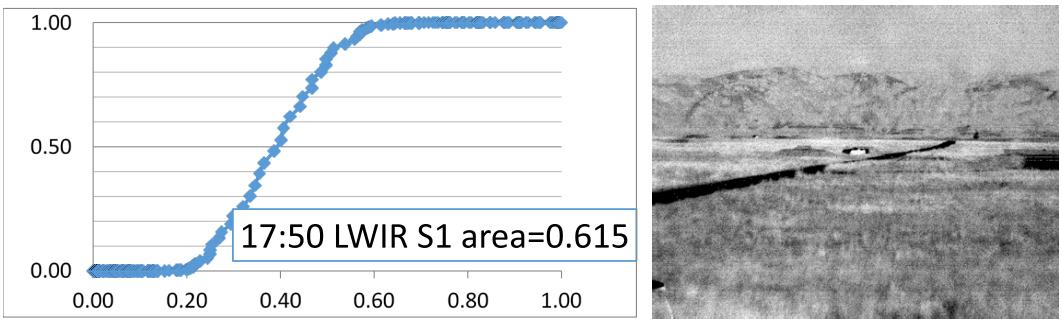

Fig. 10 ROC curve (left) and corresponding LWIR S1 image recorded at 17:50

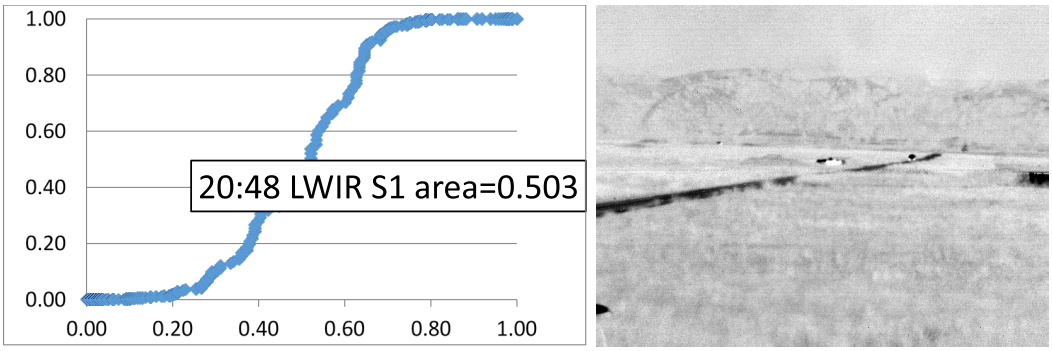

Fig. 11 ROC curve (left) and corresponding LWIR S1 image recorded at 20:48

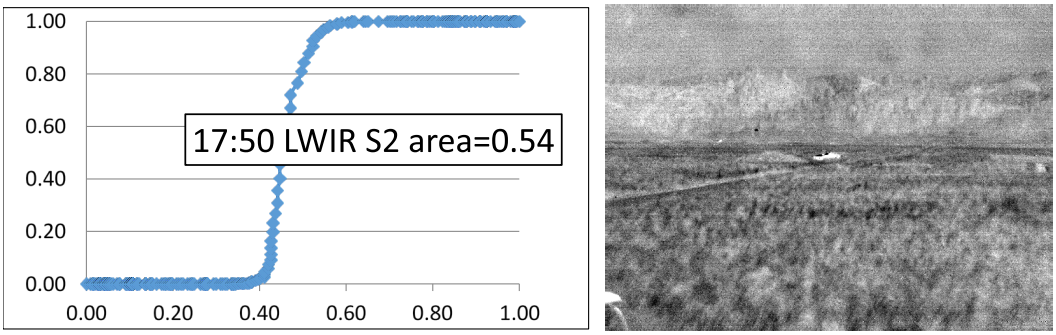

Fig. 12 ROC curve (left) and corresponding LWIR S2 image recorded at 17:50

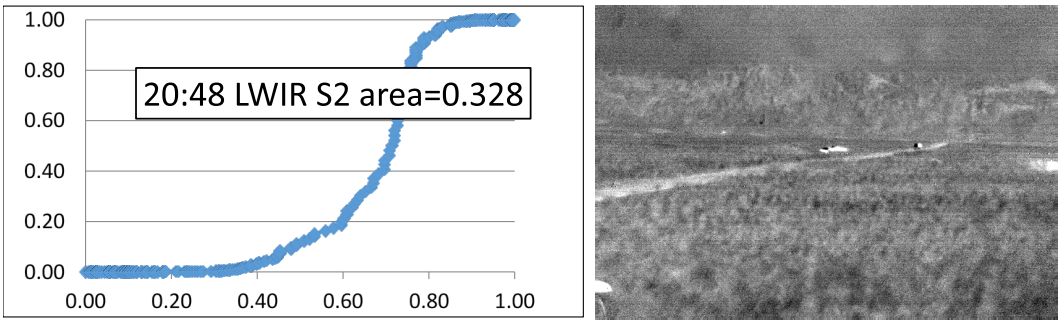

Fig. 13 ROC curve (left) and corresponding LWIR S2 image recorded at 20:48

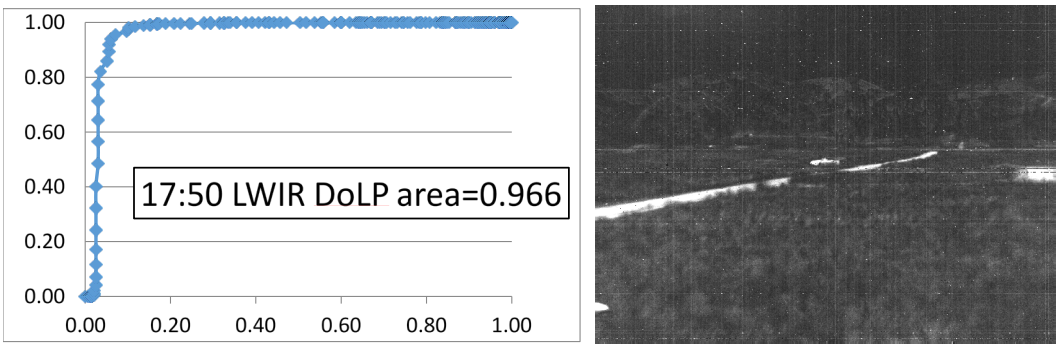

Fig. 14 ROC curve (left) and corresponding LWIR DoLP image recorded at 17:50

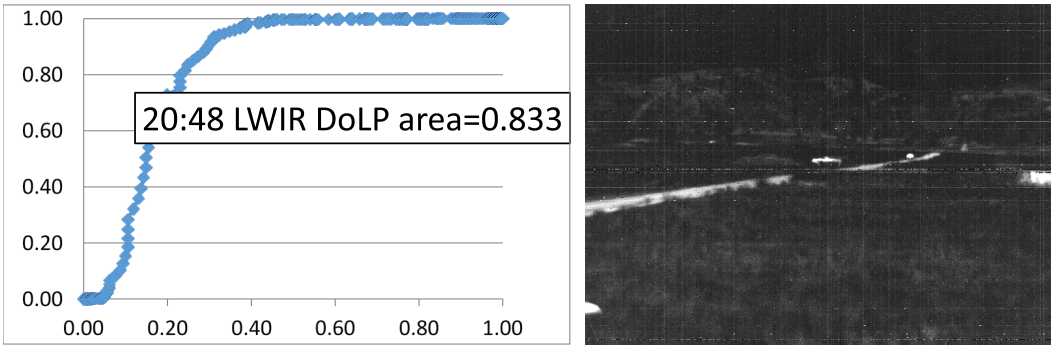

Fig. 15 ROC curve (left) and corresponding LWIR DoLP image recorded at 20:48

MidIR Results

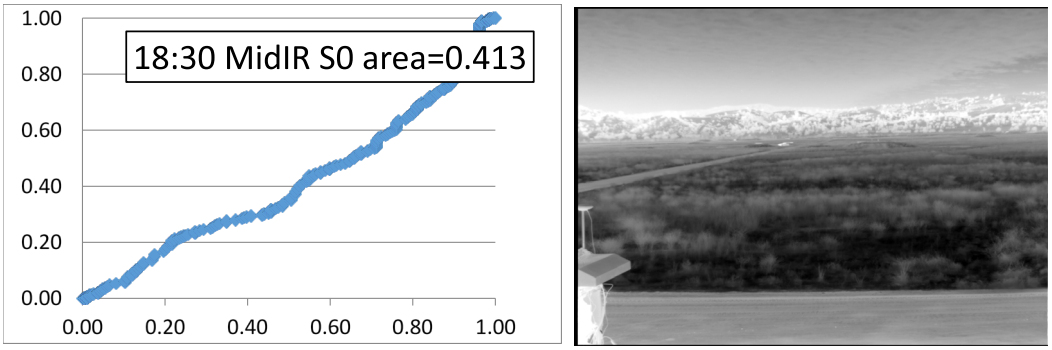

Fig. 16 ROC curve (left) and corresponding MidIR S0 image recorded at 18:30

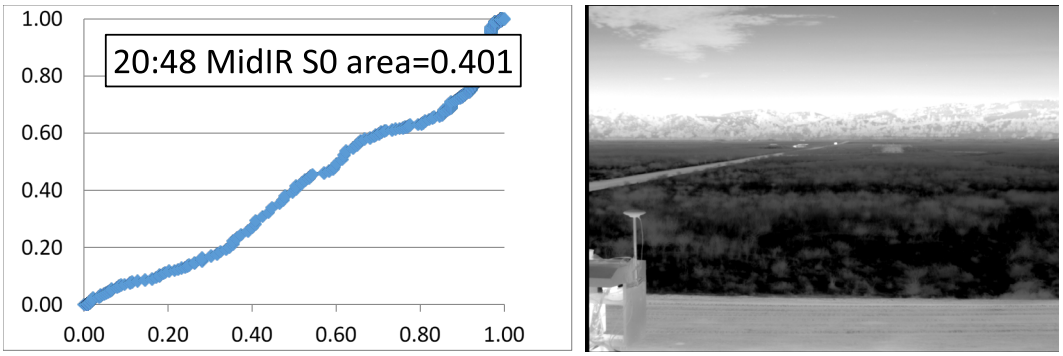

Fig. 17 ROC curve (left) and corresponding MidIR S0 image recorded at 20:48

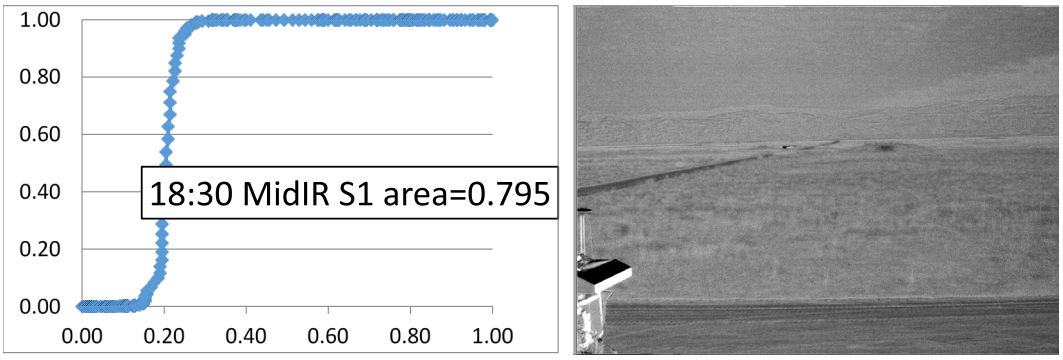

Fig. 18. ROC curve (left) and corresponding MidIR S1 image recorded at 18:30

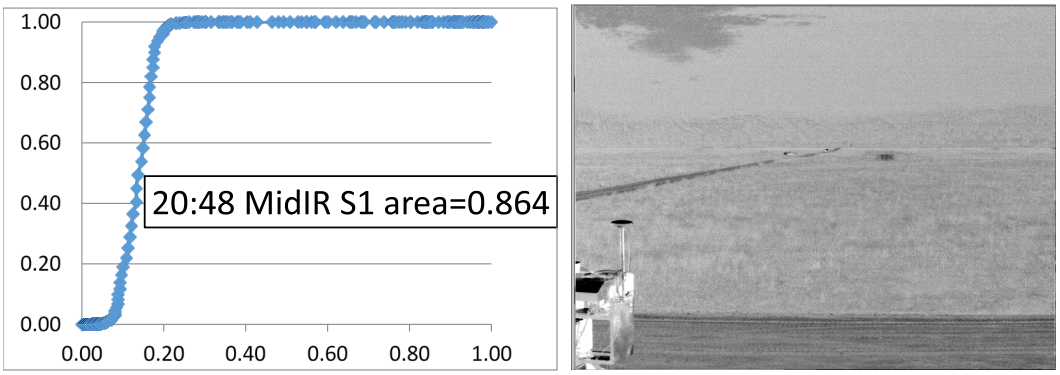

Fig. 19 ROC curve (left) and corresponding MidIR S1 image recorded at 20:48

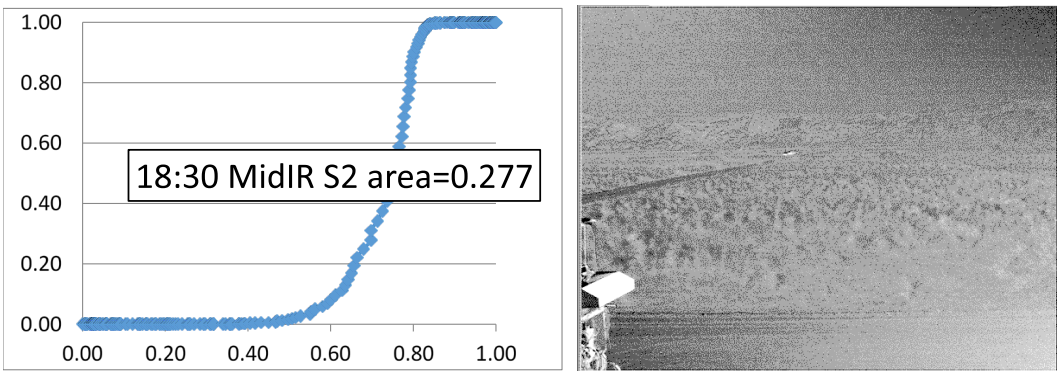

Fig. 20 ROC curve (left) and corresponding MidIR S2 image recorded at 18:30

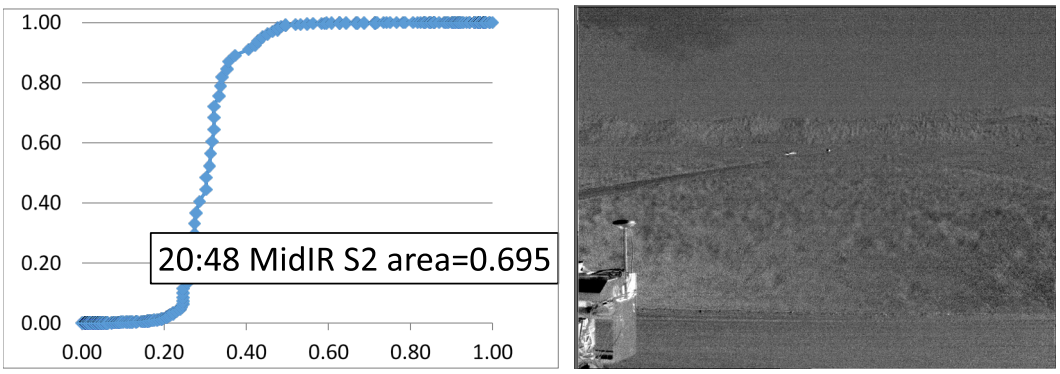

Fig. 21 ROC curve (left) and corresponding MidIR S2 image recorded at 20:48

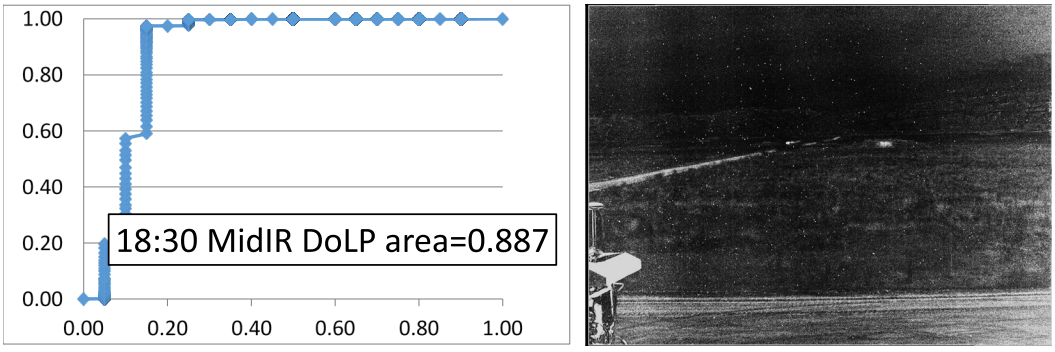

Fig. 22 ROC curve (left) and corresponding MidIR DoLP image recorded at 18:30

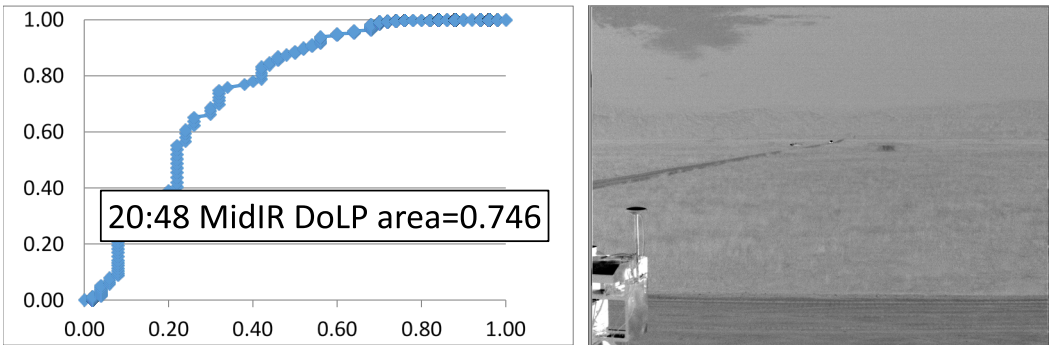

Fig. 23 ROC curve (left) and corresponding MidIR DoLP image recorded at 20:48

7. Results and Conclusion

The results of Figs. 8–23 are summarized in Table 3. As seen in Fig. 8, the target in question (i.e., a T-72 tank at 17:50) is clearly detectable in the LWIR radiance image S0, resulting in a detection probability of 78%. This undoubtedly is due to the relatively high ambient temperature (compared to background) of the tank due to solar heating as it sat in the field during the afternoon. Nevertheless, the corresponding detection probability for the DoLP image at 17:50 is seen to be 98%. This improvement of 20% results from the fact that typically in a polarimetric image, natural background clutter that exhibits little to no polarization is greatly suppressed, allowing a search algorithm to more rapidly converge onto a target.

Table 3 Results of ROC curve analysis for early evening and late evening, for all radiance and polarimetric imagery shown in Figs. 8–23

	Probability of detection (early evening)	Probability of detection (late evening)
S0 LWIR	78%	16%
S1 LWIR	61%	50%
S2 LWIR	54%	33%
DoLP LWIR	97%	83%
S0 MidIR	41%	40%
S1 MidIR	79%	86%
S2 MidIR	28%	70%
DoLP MidIR	88%	75%

However, as the evening went on and the T-72 began to cool to temperatures approaching the corresponding background, target detection within the radiant S0 image deteriorated, resulting in a detection probability of 16% at 20:48. In contrast, since a polarimetric image does not rely on temperature difference between target and background, but rather polarization differences between the target and background, the corresponding DoLP image at 20:48 exhibited an extremely high probability for detection with a value of 97%. Again, this was attributed to the

continued suppression of natural background clutter producing, in some cases, what might be described as a “binary” image.

However, for the MidIR band, detection for the radiant S0 imagery for both early and late evening data showed a detection probability of 41% and 40%, respectively. This is not unexpected, since it well known that MidIR imaging systems perform best for detection of high-temperature targets, while LWIR systems offer greater sensitivity for targets at conventional terrestrial ambient temperatures (e.g., 30–100 °F).

It should be noted, for the MidIR band, the addition of polarimetric information greatly improved probability of detection for all Stokes and DoLP images considered, with a maximum probability of detection for the early evening DoLP of 88%. Again, we attribute this to the suppression of background clutter that improves detection algorithm efficiencies. This particular aspect was unexpected and suggests that MidIR camera systems may be more effective for detection operations for ambient temperature environments if polarimetric information is considered.

During this test, we noticed something quite interesting that was not apparent in prior studies. Shown in Fig. 24 are the measured DoLP values for the T-72 for both wavebands as a function of time and are among the lowest DoLP values that we have ever recorded for a manmade target. As one can see, the measured target DoLP values are consistently less than 0.001 (or 1%) recorded throughout the test period. In all prior studies, we have rarely seen DoLP values for manmade objects less than 3%–4%, and often 8%–10% for LWIR DoLP values for typical targets at temperatures above 60 °F.[9,11,13,14]

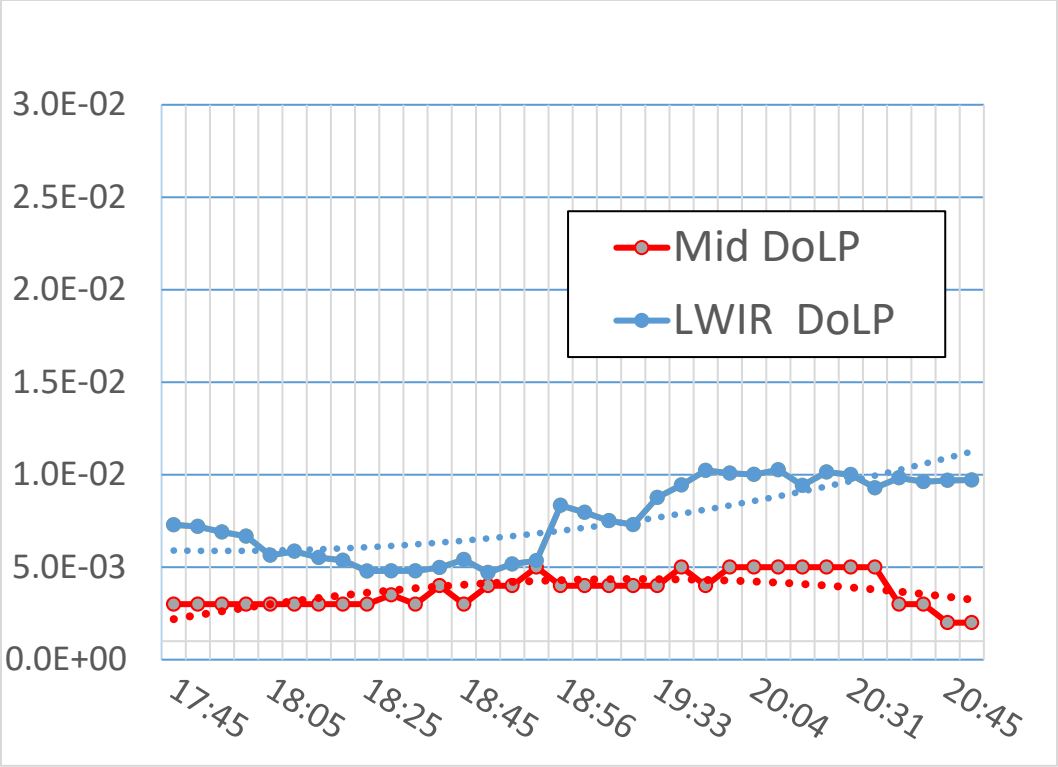

Fig. 24 DoLP as a function of time for both MidIR and LWIR wavebands and corresponding trend lines (dashed curve)

At first glance, one might associate the consistently low DoLP values with the relatively cool temperatures exhibited during the measurement (i.e., 37–49 °F), but that alone would not explain the apparent suppression of measured linear polarization.

Rather, we believe the main reason for low DoLP values arises from the fact that during the test, the target was partially illuminated by the warm distant background mountains (see Figs. 8 and 9 for examples), which were apparent for both wavebands. Plots of the radiance values for the tank target, background, sky radiance, and mountain radiance ($W/(sr*m^2)$) are shown in Figs. 25 and 26. These plots show that tank radiance was often similar, or lower, than the corresponding radiance due to the illuminating sky and/or mountain radiance values. As a result, we attribute the low recorded DoLP values to the fact that induced polarization due to "reflection" or "emission" effectively cancel one another, as explained in Section 3, Eq. 9. Nevertheless, although the DoLP values appear unusually low, detection via the ROC curve algorithm shows consistent enhancement in both the MidIR and LWIR when polarimetric information is augmented with conventional thermal imaging.

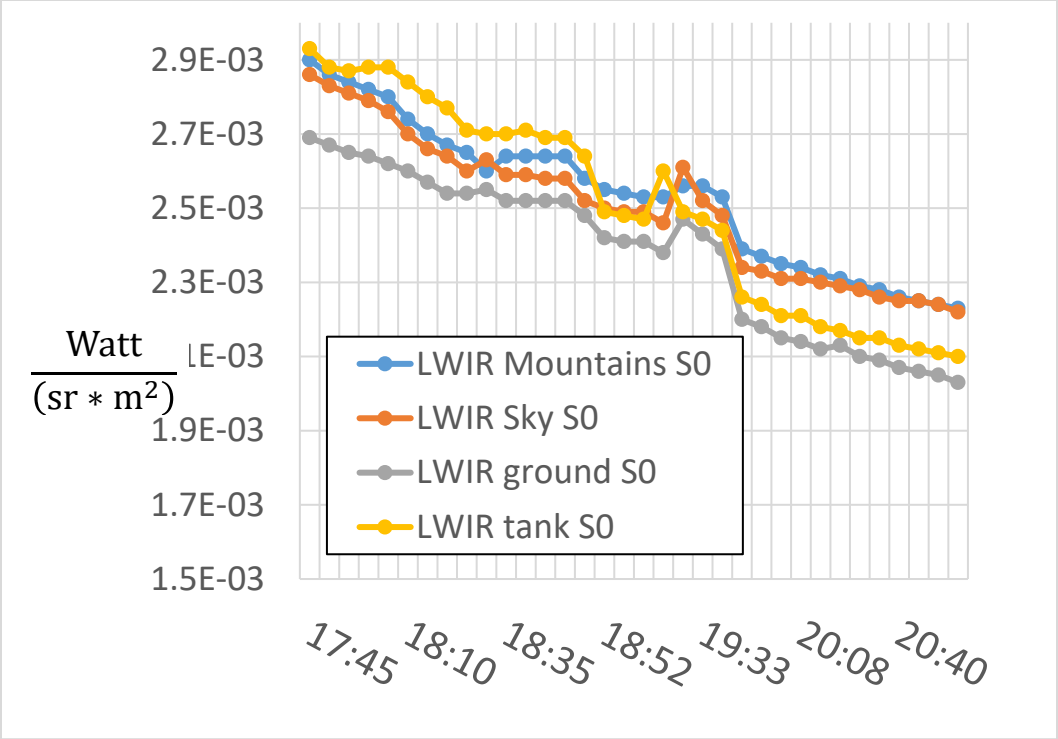

Fig. 25 Measured LWIR background and target radiance values (W/sr*m²) as a function of time recorded during January 23, 2020

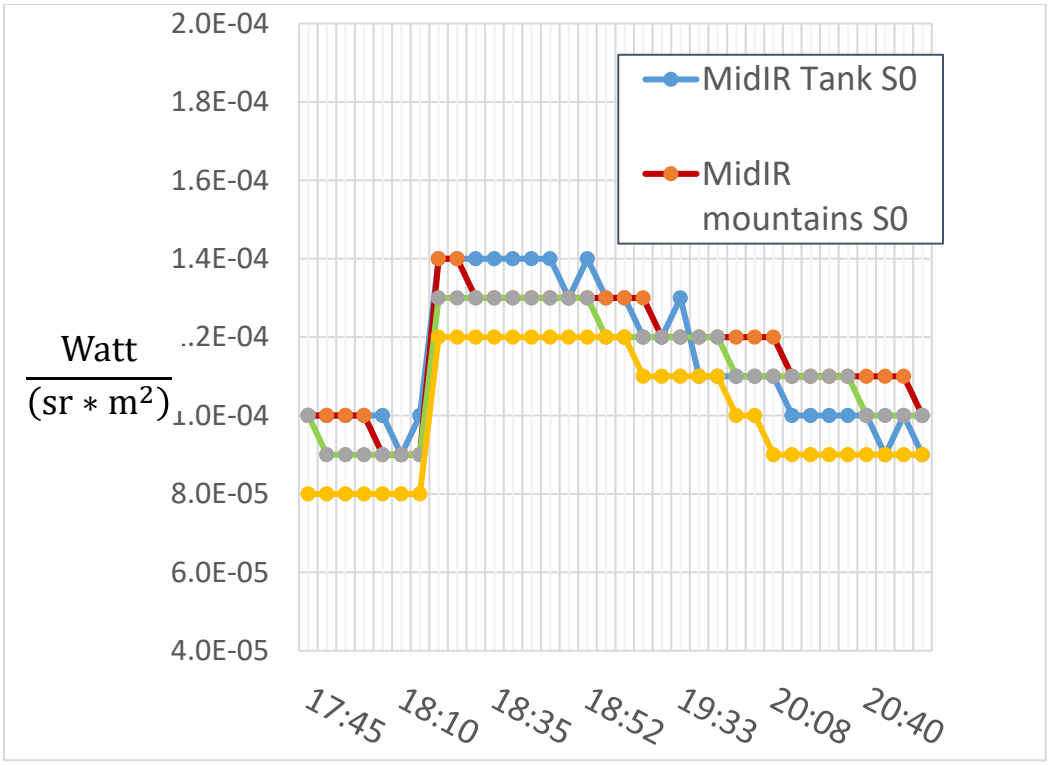

Fig. 26 Measured MidIR background and target radiance values (W/sr*m²) as a function of time recorded during January 23, 2020

8. References

1. Sandus O. A review of emission polarization. Appl Opt. 1965;4:1634–1642.
2. Walraven R. Polarization imagery. Opt Eng. 1981;20:14–18.
3. Wolfe J, Chipman RA. High-speed imaging polarimeter. In: Shawand JA, Tyo JS, editors. Polarization science and remote sensing. Proc SPIE 5158. 2003;24–32.
4. Tyo JS, Goldstein D, Chenault D, Shaw J. Review of passive polarimetry for remote sensing applications. Appl Opt. 2006;45(22):5453–5469.
5. Kudenov M, Pezzaniti L, Grant G. Microbolometer-infrared imaging Stokes polarimeter. Opt Eng. 2009 June;48(6).
6. Pezzaniti JL, Chenault DB. A division of aperture MWIR imaging polarimeter. Proc SPIE 5888. 2005;58880V.
7. Farlow CA, Chenault DB, Spradley KD, Gulley MG, Jones MW, Persons CM. Imaging polarimeter development and application. In: Goldstein DH, Chenault DB, Egan W, Duggin MJ, editors. Polarization analysis and measurement IV. Proc SPIE 4819. 2001;118–125.
8. Bowers D, Boger JK, Wellens LD, Black WT, Ortega SE, Ratliff BM, Fetrow MP, Hubbs JE, Tyo JS. Evaluation and display of polarimetric image data using long-wave cooled micro-grid focal plane arrays. In: Goldstein DH, Chenault DB, editors. Polarization: measurement, analysis, and remote sensing VII. Proc SPIE; 2006;6240:6240OF.
9. Gurton KP, Felton M. Detection of disturbed earth using passive LWIR polarimetric imaging. Proc SPIE Optics and Photonics Conference; 2009 Aug 2–6; San Diego, CA.
10. An C, Grantham J, King J, Robinson J, Pezzaniti L, Gurton K. Utility of polarization sensors for clutter rejection. 6th Annual US Missile Defense Conference; 2008 Mar 31–Apr 3; Washington, DC.
11. Gurton KP, Felton M. Detection of buried improvised explosive devices (IED) using passive long-wave infrared (LWIR) polarimetric imaging. Adelphi (MD): Army Research Laboratory (US); 2009 Sep. Report No.: ARL-TR-4941.

12. Harchanko JS, Chenault DB, Farlow CF, Spradley K. Detecting a surface swimmer using long wave infrared imaging polarimetry. In: DeWeert MJ, Saito TT, editors. Photonics for port and harbor security. Proc SPIE 5780. 2005.

13. Gurton KP, Yuffa A, Videen G. Enhanced facial recognition for thermal imagery using polarimetric imaging. Opt Lett. 2014;39(13):3857–3859.

14. Gurton KP, Felton M, Pezzaniti L. Remote detection of buried land-mines and IEDs using LWIR polarimetric imaging. Opt Express. 2012;20(20):22344–22359.

15. Gurton KP, Felton M, Mack R, Farlow C, Pezzaniti L, Kudenov MW, LeMaster D. MidIR and LWIR polarimetric sensor comparison study. Proc SPIE, Polarization: Measurement, Analysis, and Remote Sensing IX. 2010;7672:0277–786.

16. Hecht E, Zajac A. Optics. Reading (MA): Addison-Wesley; 1979.

17. Fawcett T. An introduction to ROC analysis. Pattern Recognit Lett. 2006;27:861–874.

18. Bradley AP. The use of the area under the ROC curve in the evaluation of machine learning algorithms. Pattern Recognit. 1997;30:1145–1159.

19. Gohagan JK, Spitznagel EL, McCrate MM, Frank TB. ROC analysis of mammography and palpation for breast screening. Invest Radiol. 1984;19:587–92.

List of Symbols, Abbreviations, and Acronyms

2-D	two-dimensional
DoA	division-of-amplitude
DOD	Department of Defense
DoLP	degree-of-linear polarization
FN	false negative
FOV	field of view
FPA	focal-plane array
IFOV	instantaneous FOV
InSb	indium antimonide
IR	infrared
LWIR	long-wave IR
MCT	mercury cadmium telluride
MidIR	Mid-IR
NEDT	noise equivalent differential temperature
NEDoLP	noise equivalent DoLP
NIR	near IR
ROC	receiver operating characteristic
ROI	region of interest
SAR	spinning-achromatic retarder
TN	true negative
TP	true positive

1 (PDF)	DEFENSE TECHNICAL INFORMATION CTR DTIC OCA
1 (PDF)	CCDC ARL FCDD RLD DCI TECH LIB
1 (PDF)	CCDC ARL FCDD RLC ES K GURTON